Microfluidics-based analysis of dynamic contact angles relevant for underground hydrogen storage

van Rooijen, Willemijn; Hashemi, Leila; Boon, Maartje; Farajzadeh, Rouhi; Hajibeygi, Hadi

DOI
10.1016/j.advwatres.2022.104221

Publication date
2022

Document Version
Final published version

Published in
Advances in Water Resources

Citation (APA)
van Rooijen, W., Hashemi, L., Boon, M., Farajzadeh, R., & Hajibeygi, H. (2022). Microfluidics-based analysis of dynamic contact angles relevant for underground hydrogen storage. *Advances in Water Resources*, *164*, Article 104221. https://doi.org/10.1016/j.advwatres.2022.104221

Advances in Water Resources 164 (2022) 104221

Contents lists available at ScienceDirect

Advances in Water Resources

journal homepage: www.elsevier.com/locate/advwatres

Microfluidics-based analysis of dynamic contact angles relevant for underground hydrogen storage

Willemijn van Rooijen *, Leila Hashemi, Maartje Boon, Rouhi Farajzadeh, Hadi Hajibeygi

Faculty of Civil Engineering and Geosciences, Delft University of Technology, P.O. Box 5048, Delft, 2600 GA, The Netherlands

ARTICLE INFO

Keywords:
Underground hydrogen storage
Dynamic contact angle
Wettability
Microfluidics
Hysteresis

ABSTRACT

Underground Hydrogen Storage (UHS) is an attractive technology for large-scale (TWh) renewable energy storage. To ensure the safety and efficiency of the UHS, it is crucial to quantify the H_2 interactions with the reservoir fluids and rocks across scales, including the micro scale. This paper reports the experimental measurements of advancing and receding contact angles for different channel widths for a H_2/water system at P = 10 bar and T = 20 °C using a microfluidic chip. To analyse the characteristics of the H_2 flow in straight pore throats, the network is designed such that it holds several straight channels. More specifically, the width of the microchannels range between 50 μm and 130 μm. For the drainage experiments, H_2 is injected into a fully water saturated system, while for the imbibition tests, water is injected into a fully H_2-saturated system. For both scenarios, high-resolution images are captured starting the introduction of the new phase into the system, allowing for fully-dynamic transport analyses. For better insights, N_2/water and CO_2/water flows were also analysed and compared with H_2/water. Results indicate strong water-wet conditions with H_2/water advancing and receding contact angles of, respectively, 13°–39°, and 6°–23°. It was found that the contact angles decrease with increasing channel widths. The receding contact angle measured in the 50 μm channel agrees well with the results presented in the literature by conducting a core-flood test for a sandstone rock. Furthermore, the N_2/water and CO_2/water systems showed similar characteristics as the H_2/water system. In addition to the important characterization of the dynamic wettability, the results are also crucially important for accurate construction of pore-scale simulators.

1. Introduction

The contribution of renewable energy, especially wind and solar, in the future global energy mix is expected to increase significantly (MacKay, 2008). The intermittent nature of these energy resources makes the development of large-scale (TWh) energy storage facilities an essential component of future green energy systems (Heinemann et al., 2021). Hydrogen (H_2) is considered an attractive energy carrier because of its high energy content per mass, and its clean combustion products. However, because of its low density, being the tiniest molecule, surface-based storage facilities do not offer the volumes required for large-scale (TWh) energy storage. Geological formations, such as depleted oil and gas reservoirs, aquifers and salt caverns have proven to provide safe storage options for gasses such as methane and carbon dioxide, and could also offer potential solutions for hydrogen storage (Hashemi et al., 2021a; Ali et al., 2021; Zivar et al., 2020; Heinemann et al., 2021).

The feasibility of underground hydrogen storage in porous reservoirs highly depends on the flow and transport behaviour of hydrogen during subsequent injection and withdrawal cycles in the reservoir, which is governed by complex pore-scale processes (Hashemi et al., 2021b; Rücker et al., 2019; Kunz et al., 2018; Pan et al., 2021; Carden and Paterson, 1979; Heinemann et al., 2021). A common approach to investigate the impact of pore-scale processes on continuum-scale behaviour, as well as to derive meaningful continuum-scale transport parameters such as relative permeability and capillary pressure, is pore-network modelling (Blunt et al., 2002; Joekar-Niasar and Hassanizadeh, 2012; Celia et al., 1995; Constantinides and Payatakes, 1996; Oren et al., 1998; Patzek, 2001). In pore-network modelling the relevant physics at the pore-scale (e.g., contact angles and interfacial tension) is explicitly taken into account. However, for pore-network models to be successful, representative models of the pore-structure of the porous medium are required, as well as accurate descriptions of the wettability of the system (Dong et al., 2008; Ryazanov et al., 2009; Øren and Bakke, 2003). The wettability can be then characterized by the contact angle between the H_2/brine/rock interfaces (Section 2.1, Fig. 1) (Hashemi et al., 2021b; Blunt, 2017; Bear, 2013). The contact

---

* Corresponding author.
E-mail address: w.a.vanrooijen@tudelft.nl (W. van Rooijen).

https://doi.org/10.1016/j.advwatres.2022.104221
Received 2 February 2022; Received in revised form 2 May 2022; Accepted 2 May 2022

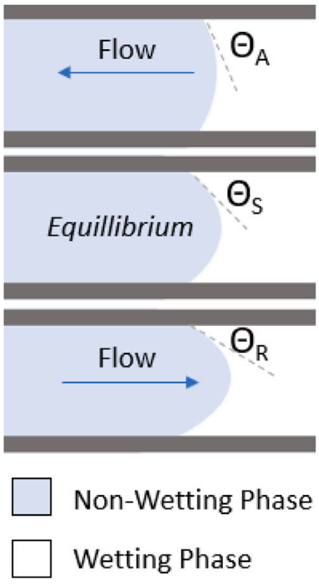

Fig. 1. Schematic drawing showing the interface between the wetting and non-wetting phase. The advancing (ACA) and receding contact angles (RCA) are indicated by Θ_A and Θ_R, respectively. The static contact angle is also illustrated by Θ_S.

angle is a function of, among other factors, pore size and pore geometry (Behnoudfar et al., 2022; Rabbani et al., 2016, 2017). Furthermore, the contact angle can potentially be different during drainage and imbibition cycles, even in tube-like channels, used in pore-network systems. This phenomena is known as the contact angle hysteresis. Contact angle hysteresis is the result of the pore-structure heterogeneity, chemical interactions between the fluid and solid rock surface, as well as surface roughness (Behnoudfar et al., 2022; Sauer and Carney, 1990; Tadmor, 2004). Contact angle hysteresis has a direct impact on the amount of residual and capillary-trapped non-wetting phase (Juanes et al., 2006), in this case H_2, and the economic feasibility of UHS, as the trapped H_2 cannot be produced from the reservoir.

Contact angles can be directly measured experimentally using the Captive bubble method (Hashemi et al., 2021b; Saraji et al., 2014), Sessile drop method (Dickson et al., 2006; Espinoza and Santamarina, 2010; Dalton et al., 2020), Capillary tubes (Li et al., 2013; Heshmati and Piri, 2014; Al-Zaidi and Fan, 2018; Castro et al., 2018), Tilted plate method (Arif et al., 2017), Wilhelmy plate method (Kim et al., 2015), Microfluidic chips (Jafari and Jung, 2017; Castro et al., 2018), and In-situ μCT measurements (Dalton et al., 2020; Sun et al., 2020; Alhammadi et al., 2017; Higgs et al., 2022), of which μCT measurements of the contact angles are most representative of local pore geometries.

Morrow (1975) studied the dependence of the advancing and receding contact angles on intrinsic contact angles. The intrinsic contact angles were measured on a smooth PTFE surface, for different fluid pairs. However, importantly to note, the corresponding advancing and receding contact angles were measured in roughened PTFE tubes. Under these conditions, Morrow (1975) showed a systematic dependency of the advancing and receding contact angles on the intrinsic contact angle. Note that on smooth surfaces no hysteresis was expected to be observed. As such, the advancing and receding contact angles for smoothed surfaces were assumed to be equal to the intrinsic contact angle. It is, therefore, expected that in the relatively new pore-scale simulation studies, Morrow's curves have been modified to obtain meaningful simulations (Hashemi et al., 2021a). In general, there are only limited experimental data sets available for H_2/water contact angles in porous reservoirs. Moreover, no direct measurements to quantify the effect of pore size/channel width on this parameter have been reported. Furthermore, no direct measurement of H_2 dynamic contact angles in tube-like micro channels have been done. The analyses of hydrogen transport properties in tube-like channels sheds new lights on meaningful design of pore-scale network simulation frameworks.

Relevant to UHS, in the literature, some experimental studies to characterize hydrogen transport properties have been conducted. Yekta et al. (2018) performed core-flooding tests, in which hydrogen was injected into a water-saturated Vosges sandstone rock, to derive drainage relative permeability and capillary pressure curves. The experiments were carried out to represent shallow (50 bar – 20 °C) and deep (100 bar – 45 °C) aquifers. By combining the capillary pressure results with mercury injection capillary pressure (MICP) measurements and using the Young–Laplace scaling, they found the receding contact angles of 21.6° and 34.9° for the first and second conditions, respectively. Iglauer et al. (2021) used the tilted plate experimental technique to determine advancing and receding contact angles for the H_2/brine/quartz system. The experiments were performed for a pressure range of 50–250 bar, and a temperature range of 23–70 °C. A brine with a salinity of 100,000 ppm NaCl was used. They found that increasing pressure, temperature, and organic surface concentration increased the hydrogen wettability, with contact angles ranging between 0° to maximum 50°. Hashemi et al. (2021b, 2022) performed direct static contact angle measurements for H_2/brine/sandstone rock using a captive-bubble cell device. No correlations between the static contact angle and the pressure (20–100 bar), temperature (20–50 °C) and salinity (0 – 50 000 ppm NaCl) of the brine were found. Intrinsic contact angles between 25° (min) to 45°(max) were found for a variety of tests. Most recently, Higgs et al. (2022) determined wettability of H_2/brine/quartz systems, using captive bubble, pendant drop and in-situ 3D micro-CT methods. They found contact angles of 29°–39° at pressures of 69–210 bar and salinities of 0–5000 ppm NaCl. Consistent with the earlier findings (Hashemi et al., 2021b), in their results, no conclusive impact of salinity or pressure was observed on the contact angle. Although, water-wet conditions were commonly found in all the past experiments, a wide variation in the currently reported H_2/brine contact angle data exists. This could possibly be explained by differences in the measurement techniques, where pore size/channel width could play a defining factor.

In order to provide valuable and missing wettability information for pore-network models, as well as to improve the scientific community's understanding of currently reported data on H_2/brine contact angles, in this work, we present a systematic study to measure H_2/brine contact angles for different channel widths in microfluidic systems for both drainage (receding) and imbibition (advancing) processes.

Experimental microfluidic investigations can provide insight in the dynamics of pore-scale processes (Porter et al., 2015; Karadimitriou and Hassanizadeh, 2012), and provide a bridge between the pore and the core scale (Karadimitriou et al., 2019). Microfluidic experiments at early stages were based on simple micromodels, but later involved more complex network geometries (Porter et al., 2015). The main limitations of most micromodels to represent actual subsurface systems, however, include their restriction to 2D networks, with a uniform etch depth in the third dimension, uniform surface chemistry and minimum channel width of 10 μm (Kim et al., 2012). There are a few examples of micromodels which resemble actual 3D rock systems more closely (Gunda et al., 2011; Song et al., 2014). Micromodels have widely been used for experiments on the fundamentals of multiphase flow (Godinez-Brizuela et al., 2017; Cheng et al., 2004), transport (Karadimitriou et al., 2016, 2017) and wettability (Sharbatian et al., 2018; Kim et al., 2012; Chalbaud et al., 2009; Hu et al., 2017; Jafari and Jung, 2017; Karadimitriou et al., 2019). Micromodels can, for example, be used to simulate drainage and imbibition processes and to study underlying processes like viscous or capillary fingering and snap-off (Gutiérrez et al., 2008; Ferer et al., 2004; Zhang et al., 2011; Joekar Niasar et al., 2009). The complex pore-geometries in real rocks make it difficult to systematically analyse the impact of factors such as pore size on the in-situ contact angle measurements (Higgs et al., 2022; Alhammadi

Table 1
Summary of the test groups and experimental conditions.

Test Group	Gas	Liquid	Rate [μl/min]	Temperature [°C]	Pressure [bar]
A	H_2	Pure Water	0.1	20	10
B	N_2	Pure Water	0.1	20	10
C	CO_2	Saturated Water	0.1	20	10

et al., 2017). The advantage of using microfluidic chips is that the in-situ dynamic contact angles can be measured in simplified systems but with channel widths that are representative of porous media in the subsurface formations. However, to the best of the authors' knowledge, no study has been reported, in which micromodels are used to directly measure dynamic contact angles of H_2/brine systems.

The objective of this work is to characterize dynamic contact angles for different channel widths in a H_2/water/glass microfluidic system. In addition, the experiments will be carried out for CO_2 and N_2 to allow for the comparison with more commonly stored gasses in subsurface reservoirs. The results reported in this study can directly be used to take into account the impact of pore size/channel width on contact angle in pore-scale modelling approaches such as the one performed by Hashemi et al. (2021a), in order to find meaningful relative permeability and capillary pressure curves. Furthermore, this work can be used to improve our understanding of the wide variation in the limited H_2/brine contact angle data that is currently reported. The remainder of the paper is structured as follows. First, the experimental setup and procedure will be described, followed by the method of image analysis. Then, the results and their relevance for UHS will be provided and discussed. Finally, concluding remarks will be presented.

2. Materials and methods

In this study, microfluidic chips are utilized to measure dynamic contact angles of gas–solid–liquid interfaces for the H_2/water, N_2/water, and CO_2/water systems. The experimental test groups and conditions are summarized in Table 1.

2.1. Theory

The wettability is a measure of the ability of a fluid to interact with a solid surface in combination with another fluid, and can be represented by the contact angle. The contact angle is defined as the angle that a two-fluid interface makes with the solid surface. A contact angle bigger than 90° defines the non-wetting phase, while a contact angle smaller than 90° defines the wetting phase (Blunt, 2017; Bear, 2013). In cases where the interface is not moving, the contact angle is static (SCA). Dynamic contact angles can be measured during drainage, where the non-wetting phase is displacing the wetting phase, corresponding to the injection of hydrogen in the reservoir. The contact angles measured during drainage are receding contact angles (RCA). When the process is reversed and hydrogen is withdrawn from the reservoir, the wetting phase is displacing the non-wetting phase, which is called imbibition. The contact angles measured during imbibition are advancing contact angles (ACA). An illustration is provided in Fig. 1. Hysteresis is defined as the difference in contact angle during the drainage and imbibition phase of the process (Rapp, 2016). When the surface is smooth and the fluids are at rest and free of polar impurities, the static contact angle is a fundamental property of the system and is called the intrinsic contact angle (ICA) (Morrow, 1975).

2.2. Materials

The microfluidic device used in the experiments consisted of a microchip (10 × 20 mm) supplied by Micronit Company. The material of the chip is borosilicate glass, with a pattern of a random square network. The channels have widths of 50, 70, 90, 110 and 130 μm measured in the widest part of the channel (see Fig. 2). The width of the smallest channel is in the range of the most common pore sizes measured in Berea and Bentheimer sandstones (Hashemi et al., 2021b; Anon, 2022). The depth of the channels is 20 μm. The shape of the channels is near-rectangular, with edged sides at the bottom. The permeability of the chip is 1.6 D, which is comparable with the permeability found for Bentheimer sandstone (Peksa et al., 2015). An overview of the chip can be found in Fig. 2. H_2, N_2 and CO_2 gas with respective purity of 99.99%, 99.7% and 99.7% were used. Degassed deionized water was used during the experiments. For the CO_2 experiments the water was pre-saturated with CO_2, because of the high solubility of CO_2 in water. H_2 and N_2 solubility in water is very low, with no expected impact on the contact angle (Hashemi et al., 2022). Therefore, the water used in these experiments was not pre-equilibrated.

2.3. Experimental apparatus

Fig. 3 provides a schematic overview of the microfluidic apparatus. The microscope is a Leica DMi8 DFC7000 and was used in combination with a lens with a magnifying factor of 10. Videos of the experiments were taken with a Leica DFC7000T camera with LAS software. The frame rate of the videos was approximately 5 frames per second. The resolution of the videos was 1920 × 1440 pixels, with a pixel size of 0.75 × 0.75 μm. To prevent the chip from being contaminated, multiple filters were incorporated in the apparatus. The injected water (and ethanol) was filtered with a 0.2 μm VICI filter. In addition, there were two extra 0.5 μm filters (VICI Jour PEEK-encased frits) installed in the liquid and the gas lines. Two pumps were included in the setup, a quizix QX6000 pump and a PHD Ultra™ 4400 Programmable Syringe Pump - Harvard Apparatus with a 250 μL syringe. The Quizix pump was used to refill the highly accurate syringe pump, which can deliver flow rates as small as a few nanolitres per minute. The syringe pump was used for the injection into, and the withdrawal from, the microchip. The valves installed (Swagelok) were all 1/16" in size. Also, the tubes with 0.25 mm inner diameter (ID) with FEP transparent material were used to connect the pumps to the chip. The gas cylinder served to maintain the pressure. The pressure was monitored by the Quizix Pump. The experimental setup was limited to a pressure of 10 bar.

Safety aspects are crucially important when working with H_2. Therefore, in this study, the small volume of H_2 needed for the experiments was obtained from the gas regulator so that the gas cylinders could be closed during experiments. The volume of the regulator is approximately 99 mL, which is large enough to carry out several experiments, but small enough to pose limited safety risks in a well-ventilated lab.

The setup was calibrated against the existing literature data of Jafari and Jung (2017), in which the same chip was used to measure dynamic contact angles for the CO_2/water system. An important difference between the experimental apparatus of Jafari and Jung (2017) and the one used in this study is the presence of several filters. The filters keep the system clean and avoid any impact of impurities on the contact angle measurements. More details about the validation tests and the impact of impurities on contact angle measurements can be found in Appendices A and C.

2.4. Experimental procedure

In this study, drainage and imbibition experiments are carried out as separate experiments. The objective is to measure dynamic con-

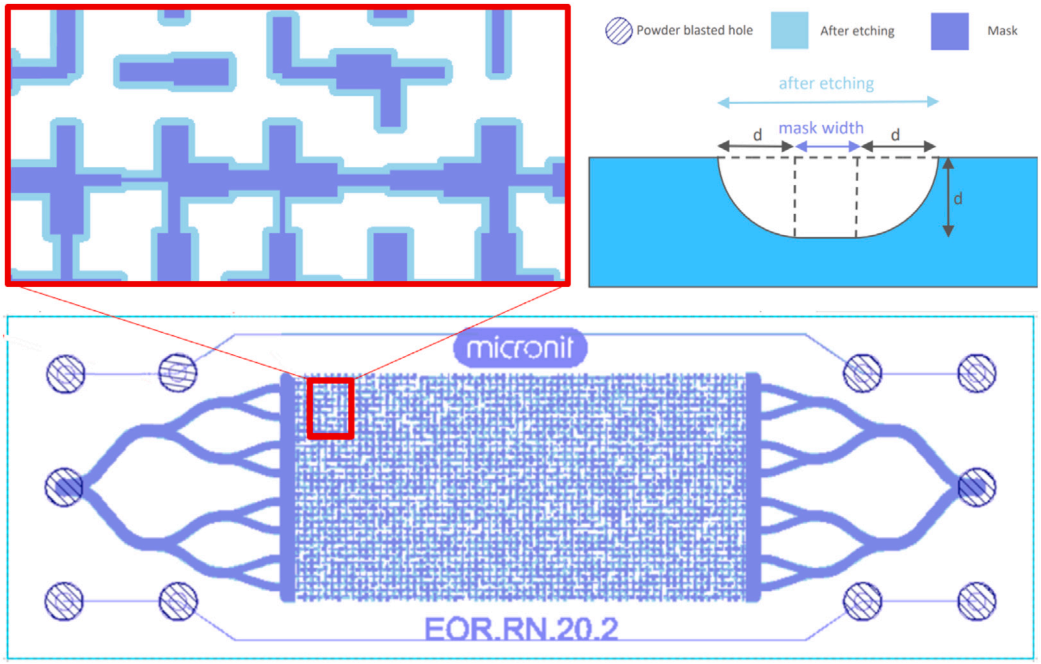

Fig. 2. Schematic drawing of the borosilicate glass chip (based on the drawing on the website of Micronit Company). The chip is 10 mm × 20 mm. The channels have widths of 50, 70, 90, 110 and 130 µm and the depth of the channels is 20 µm.

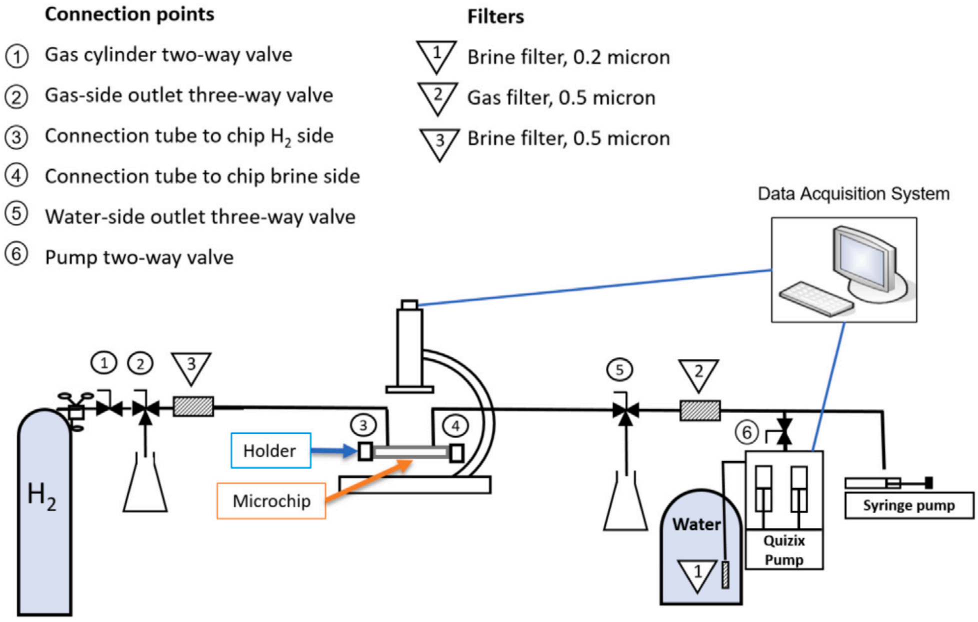

Fig. 3. Schematic drawing of the experimental apparatus used to measure dynamic contact angles in microfluidic chips.

tact angles as a function of channel width for these two different displacement processes. During the experiments, videos were taken to capture the moving gas–water interfaces within the channels. The drainage and imbibition tests were repeated until a sufficient amount of measurements for each channel width could be derived from the videos. A flow rate of 0.1 µl/min has been used during all experiments. This corresponds to an interstitial velocity (V) of $\approx 10^{-4}$ m/s. A capillary number ($Ca = \mu V/\sigma$) of $\approx 10^{-8}$ was calculated using an interfacial tension (σ) of 72.9 mN/m (Yan et al., 2001) and a dynamic viscosity (μ) of 9 µPa s (Yusibani et al., 2011), which indicates a capillary-dominated flow regime.

2.4.1. *Cleaning procedure*

Prior to each experiment, the microchips were thoroughly cleaned. The cleaning procedure involved rinsing the chips with 5 mL of filtered ethanol, followed by flushing with filtered N_2 until no liquid was visible in the chip. The cleaning procedure was carried out at ambient pressure. To remove the N_2 from the clean chip, the system was flushed

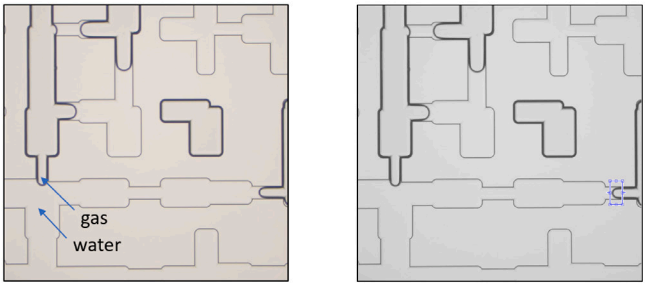

(a) Original image (b) Grey-scale image

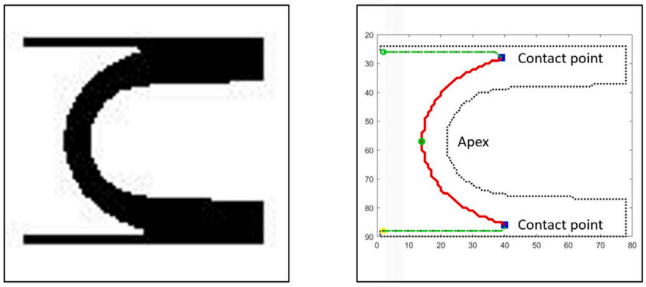

(c) Binarized and cropped image (d) Detection of interface and channel walls

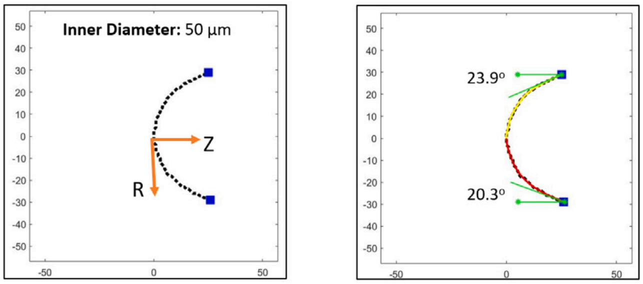

(e) Curvature from image (f) Fitted 6th order polynomial on curvature

Fig. 4. Procedure of the image analysis to identify the contact angles.

with the gas used in the experiment, followed by thoroughly rinsing with deionized water.

2.4.2. *Drainage experiments*

Before the start of the drainage experiments, the chips were saturated with deionized water at ambient pressure, after which the system was pressurized to the experimental pressure of 10 bar. However, for the experiments where the deionized water was pre-equilibrated with CO_2 (see Table 1), the system was saturated at the experimental pressure of 10 bar to avoid exolution of dissolved CO_2 from the water. For these experiments, back-pressure regulators were installed at the outlets of valve 2 and 5. The drainage experiments were conducted by withdrawing water from the fully water-saturated chips with a flow rate of 0.1 μL/min.

2.4.3. *Imbibition experiments*

Before the start of an imbibition test, the chip was flushed with the gas of the experiment until the water inlet was completely filled with gas. This forced the injected water during the imbibition experiment to flow through channels filled with gas instead of pre-existing wet flow paths, which was necessary to be able to make measurements in all channel widths. The flushing was carried out at ambient pressure, after which the pressure was increased to the experimental pressure of 10 bar, except for the experiments in which the deionized water was equilibrated with CO_2. For these experiments the flushing pressure was kept at 10 bar. The imbibition experiments were conducted by injecting water with a flow rate of 0.1 μL/min into the microchip.

2.5. *Image analysis*

To calculate the dynamic contact angles, snapshots from videos of the moving gas–water interfaces in different channel widths were captured throughout the entire chip. Snapshots were taken at locations where the interfaces met the following requirements: (1) the interface is moving, (2) the interface is not too close to the corners of the channels, and (3) the meniscus snapshot is sharp. Furthermore, only one snapshot per straight channel was taken to obtain a good representation of the whole microchip.

Interfaces which met the three requirements were analysed using an in-house code. To process an image, first it was converted to a grey-scale format and the desired interface within a channel was cropped. Then, by using the scale factor of the microscope and selecting two points on the channel walls, the channel width was identified. To detect the boundary of the meniscus, the cropped section of the image was binarized and contact points, in addition to the apex, were identified. The best polynomials on each half of the curvature were fitted by both minimizing the error at the contact points (RMSE) and choosing a polynomial that optimally fits the meniscus (Darzi and Park, 2017; Heiskanen et al., 2008). All the steps of the image analysis are shown in Fig. 4.

Contact angles are found first by fitting a polynomial of order n on the image, i.e.,

$$Z = c_1 R^n + c_2 R^{(n-1)} + c_i R^{n-(i-1)} + \cdots + c_{(n+1)}. \tag{1}$$

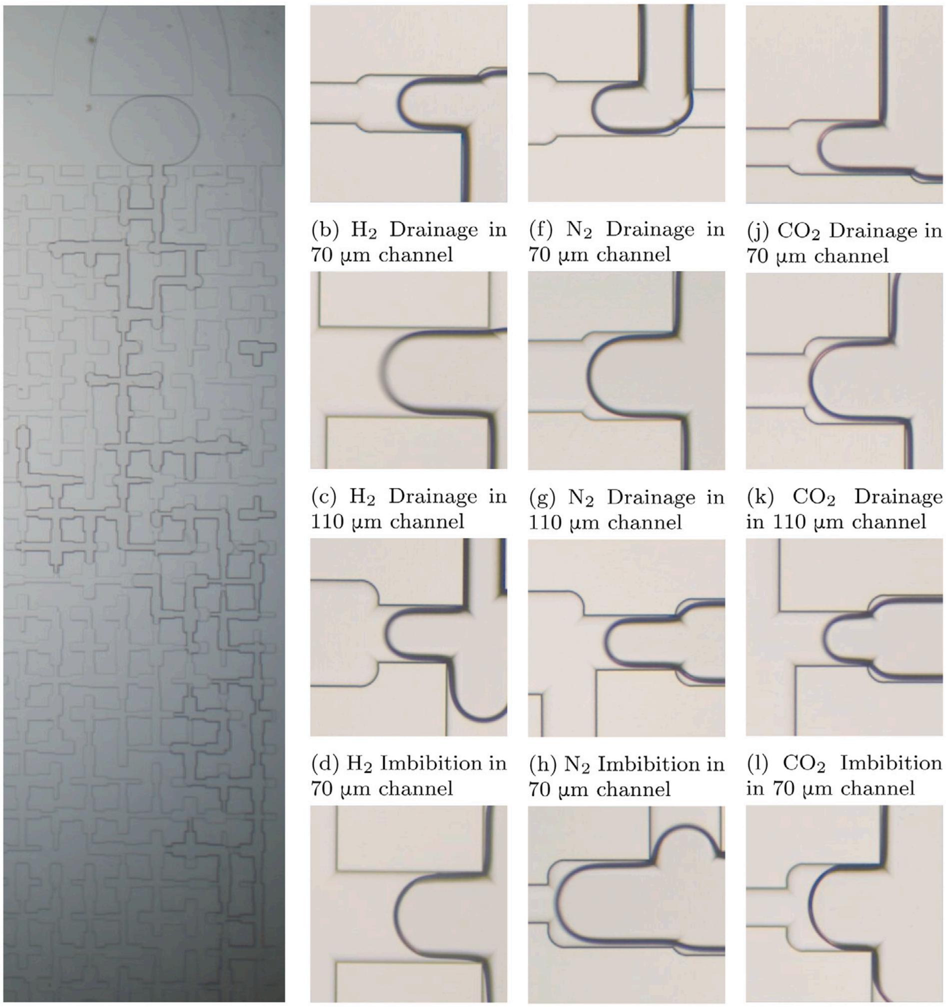

(b) H_2 Drainage in 70 µm channel
(f) N_2 Drainage in 70 µm channel
(j) CO_2 Drainage in 70 µm channel
(c) H_2 Drainage in 110 µm channel
(g) N_2 Drainage in 110 µm channel
(k) CO_2 Drainage in 110 µm channel
(d) H_2 Imbibition in 70 µm channel
(h) N_2 Imbibition in 70 µm channel
(l) CO_2 Imbibition in 70 µm channel
(a) Example of overview picture of drainage process
(e) H_2 Imbibition in 110 µm channel
(i) N_2 Imbibition in 110 µm channel
(m) CO_2 Imbibition in 110 µm channel

Fig. 5. Examples of images during experiments.

Here, c_i coefficients are constants, allowing the Z curve to be found as a function of R. Naturally, the derivative of Z with respect to R reads

$$\frac{dZ}{dR} = nc_1 R^{(n-1)} + (n-1)c_2 R^{(n-2)} + \cdots + c_{(n)}. \tag{2}$$

As such, the contact angle θ is found at the gas/liquid/solid contact point according to

$$\theta = \frac{\pi}{2} - tan^{-1}(\frac{dZ}{dR}). \tag{3}$$

As shown in Fig. 4(e), the origin of the coordinate system was placed at the apex point. The Z-axis is parallel to the flow direction and the R-axis perpendicular to the flow direction. Therefore, by solving Eqs. (1), (2) and (3), at the contact points the contact angle (θ) can be found. A validation of the image analysis code is provided in Appendix B.

3. Results

Fig. 5(a) shows an overview image of a drainage experiment for the H_2/water system at the point of breakthrough. The flow path is different during each experiment. The small images on the right-hand-side of Fig. 5 show drainage and imbibition examples used for measurement of advancing and receding contact angles for channel width of 70 µm and 110 µm. From left to right, the columns show the results for H_2, N_2 and CO_2, respectively. No significant difference between the wettability behaviour of these three gasses can be seen. However, in some cases a difference in interface properties (visibility of water films) could be observed between advancing and receding contact angles.

Table 2
Number of measurements.

Channel Width	H_2		N_2		CO_2	
	RCA	ACA	RCA	ACA	RCA	ACA
50 µm	28	18	20	14	10	12
70 µm	24	32	22	20	12	12
90 µm	22	30	22	18	14	22
110 µm	18	24	18	14	16	20
130 µm	18	12	20	8	18	22

The drainage and imbibition tests were repeated until a sufficient amount of contact angle measurements for each channel width were obtained for each of the gasses, and for both drainage and imbibition. The advancing and receding contact angles (ACA and RCA) for the H_2/water, N_2/water and CO_2/water systems at a pressure of 10 (±1) bar and a temperature of 20 (±2) °C (Test A, B and C), measured in channel widths varying from 50 to 130 µm are presented in Fig. 6. The error bars represent the standard deviation of the measurements.

Table 2 shows the number of measurements per measurement category. Based on this data, Fig. 7 was created in order to compare

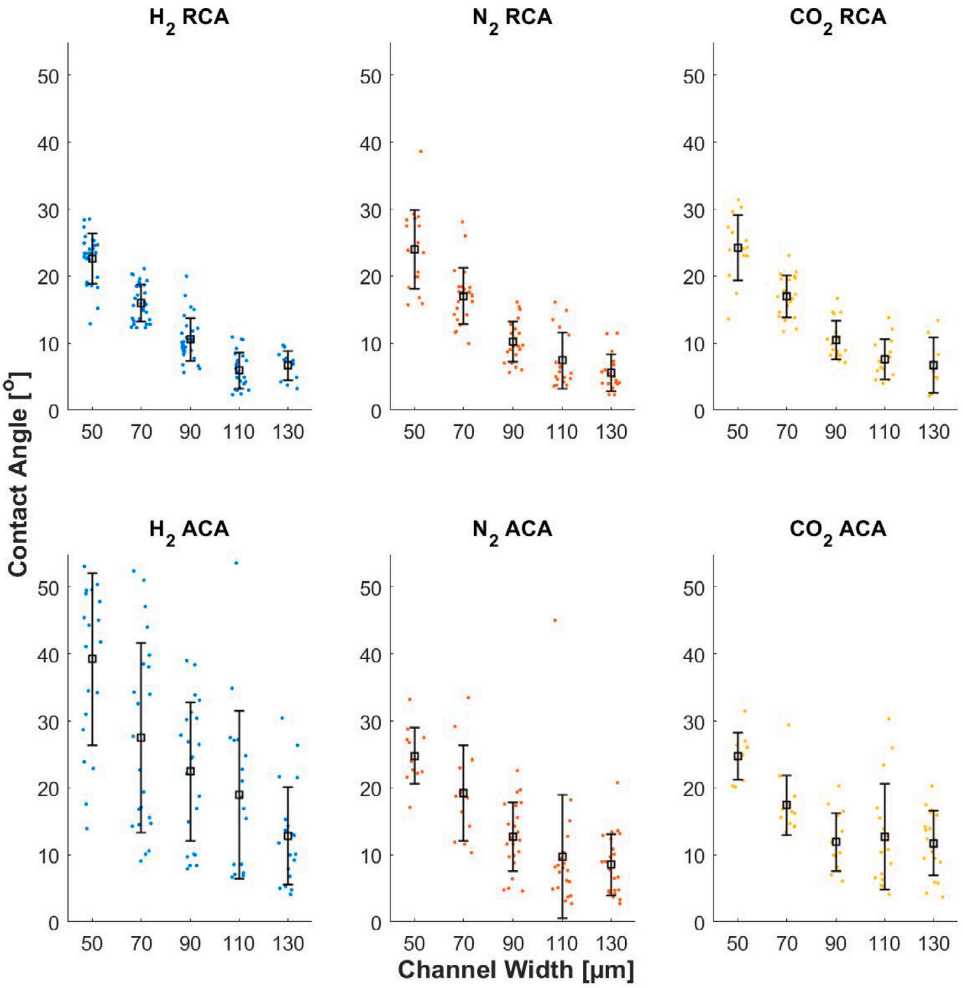

Fig. 6. All measurement points of advancing and receding contact angles (ACA and RCA) for H_2/water, N_2/water and CO_2/water systems at P = 10 bar and T = 20 °C. Pure water was used for measurements with H_2 and N_2 and for the experiment with CO_2 the water was pre-equilibrated with CO_2. The error bars represent the standard deviation of the measurements.

the results of all channel widths, gasses, and for both drainage and imbibition. The bars represent the mean values of the measurements shown in Fig. 6, and the error bars represent the standard deviation, similar to the error bars in Fig. 6. The intrinsic contact angle of H_2/water/sandstone, measured by Hashemi et al. (2021b) (P = 20 bar and T = 20 °C) is indicated by the horizontal dashed line.

H_2/water receding contact angles of 6–23° and advancing contact angles of 13–39° were determined based on the microfluidic experiments. The highest angles were measured in the smallest channels and the lowest angles were measured in the widest channels. No significant difference in the receding contact angles was observed for the three different gases. The wider spread of measurements of the advancing contact angles compared to the receding contact angles imply that the advancing contact angles are less reproducible. The advancing contact angles measured for the H_2/water system are larger (1 - 14°) compared to N_2/water and CO_2/water systems. However, the overlap in error bars shows that this difference is not evident and is within the experimental accuracy. This is because the error bars represent the standard deviation of the measurements, and the range in measurements is much larger than the measured difference between the gases.

The overlap in the error bars between advancing and receding contact angles for all cases studied indicates that there was no significant difference in the measured advancing contact angles and receding contact angles.

4. Discussion

The microfluidic system used in these experiments is not an accurate representation of a subsurface system because of the uniform etch depth, uniform surface chemistry, simplified pore network of the chip and relatively low temperature and pressure. However, the objective of the experiments is to derive contact angles for different channel widths and the random network of the microfluidic chip used in the experiments allowed for this. In order to find representative average values for each channel width, measurements were taken throughout the entire chip, taking into account a range of velocities and other effects like flow patterns. This type of systematic analysis would have been difficult to carry out in real rocks with complex pore-geometries. The experiments provide valuable information about the impact of channel width on the contact angle, which is needed for a basic understanding of tube flow, and can be used to improve the wettability characterization in pore-network modelling approaches. Pore-network models can be applied to derive meaningful continuum scale transport parameters such as relative permeability and capillary pressure by correctly taking into account the pore-scale physics. These hysteretic transport parameters are important input parameters for reservoir scale simulations methods which are needed for the optimization of underground hydrogen storage as well as to ensure its safety.

Underground hydrogen storage is relatively new compared to the much more mature technology of geological storage of CO_2. Understanding the similarities and differences between the H_2/water,

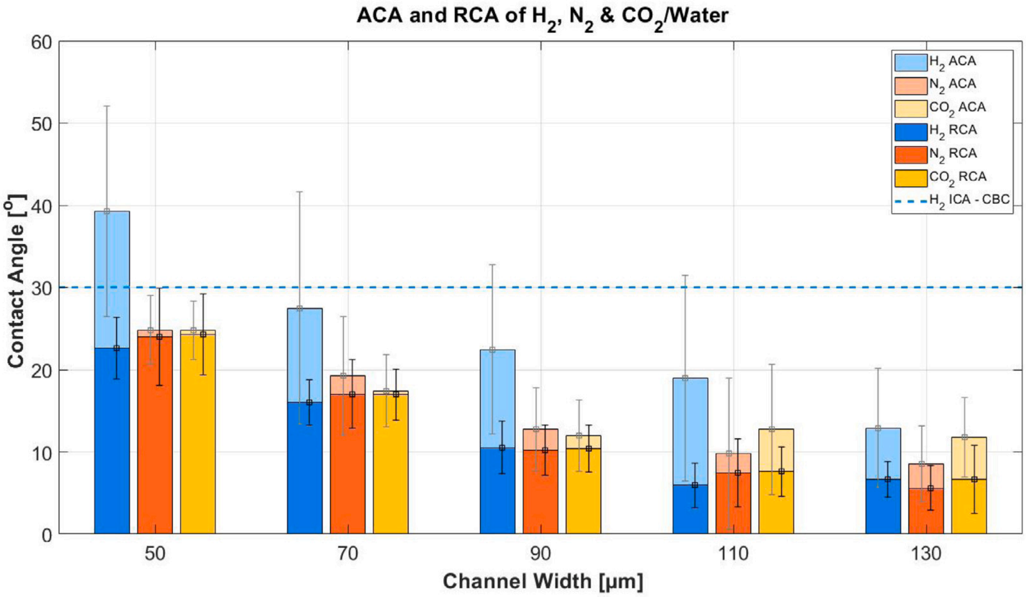

Fig. 7. Advancing and receding contact angles (ACA and RCA) for H_2/water, N_2/water and CO_2/water systems at P = 10 bar and T = 20 °C. Pure water was used for measurements with H_2 and N_2 and for the experiment with CO_2 the water was pre-equilibrated with CO_2. The dashed blue line represents the results found by Hashemi et al. (2021b) at P = 20 bar and T = 20 °C using the captive bubble cell (CBC). The error bars represent the standard deviation of the measurements.

N_2/water and CO_2/water system will help in the advancement of underground hydrogen storage, which is another objective of this study.

Because H_2 is very prone to leakage, the setup was designed such that the least amount of connections and pumps were involved. This resulted in a setup where during drainage, instead of injecting hydrogen which is the most common approach during these type of experiments, water was withdrawn. In both approaches, H_2 will first enter the pores with the lowest capillary entry pressure. When the non-wetting phase is injected, the capillary pressure ($P_c = P_{nw} - P_w$) is increased by increasing the pressure of the non-wetting phase. When the wetting phase is withdrawn as in our case, the capillary pressure is increased by lowering the pressure in the wetting phase.

4.1. Characteristics of the interface

During the drainage and imbibition experiments for H_2/water, N_2/water, and CO_2/water, different kind of interfaces were observed. The main difference was in the existence or non-existence of visible water films. It is important to mention that the term water film is used for all cases where water was observed on the channel walls of gas filled channels. Water on the channel walls can be caused by both corner flow and actual water films, but we will refer to it as water films, as we are not able to distinguish between the two. A water film is expected to be present in all cases (Hirasaki, 1991), however, in some of our cases the water film was so thin that it was not visible with the camera. During drainage, when the receding contact angles (RCA) were measured, water films were visible on both sides of the channel (Fig. 8(d)). For the measurements of advancing contact angles (ACA) during imbibition, interfaces were observed both with and without visible water films (Figs. 8(a)–8(c)). This was caused by the mainly dry channel walls at the start of the imbibition experiments. During the experiment, in some cases the walls of the channels were first covered with a water film before the interface arrived, while in other cases this effect was not visible. The differences in thickness of water films caused the spread of measurements to be bigger for advancing contact angles compared to receding contact angles. Due to the curved interface of the channel walls, as well as the limitations of the microscope and camera used, the thickness of the water film could not be measured.

Fig. 9 shows the type of interface (with or without visible water film) that was encountered at each advancing contact angle measurement for all three gasses. It can be seen that in bigger channel widths fewer measurements are without water film, since a water film can more easily enter the bigger channels. Furthermore, higher values of advancing contact angles are mainly measured without a visible water film present.

The interfaces are very sensitive to contamination within the gas/water/glass system. The differences in contact angle measurements between clean and impure systems, as well as example images of the polluting particles can be found in Appendix C.

4.2. Influence of channel width on contact angles

According to Behnoudfar et al. (2022), the contact angle (θ) is, besides the pore size (r), related to the radius of curvature of the interface (R) and the convergence angle of the pores (ϕ), by:

$$\theta = cos^{-1}\frac{R}{r} - \phi. \tag{4}$$

Because the microchip consisted of straight channels, the convergence angle in our study is equal to zero. Using this equation it can be calculated that the average radius of curvature ranges from 27 to 65 µm for the H_2/water receding contact angles and 32 to 67 µm for the H_2/water advancing contact angles. This shows that the channel width not only affects the contact angle but also the radius of curvature of the interface. In dynamic systems the radius of curvature is impacted by the velocity. In our system, a wide range of velocities were measured for each channel width. However, no systematic relationship between velocity and contact angle was observed. Furthermore, similar velocities were measured for each channel width, which suggests that the dependency of contact angle on channel width was not due to differences in velocity. Further explanation can be found in Appendix D.

The results show a relationship where dynamic contact angles increase with decreasing channel width. Similar trends have been observed in the literature for CO_2/water system (Jafari and Jung, 2017). To theoretically explain the observed behaviour, i.e., increasing contact angle with decreasing channel width, two main situations were considered on the basis of (1) equal capillary pressure in all channel widths and (2) equal average velocity in all channel widths. Both approaches

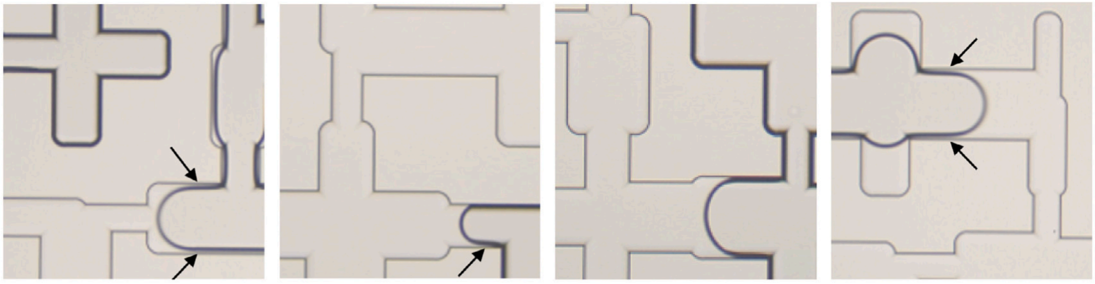

(a) ACA with water films visible on both sides (b) ACA with a visible water film on one side (c) ACA without visible water films (d) RCA with visible water films on both sides

Fig. 8. Types of interfaces encountered during imbibition when the advancing contact angle (ACA) is measured (a,b,c) and during drainage when the receding contact angle (RCA) is measured (d). The visible water films are marked with an arrow.

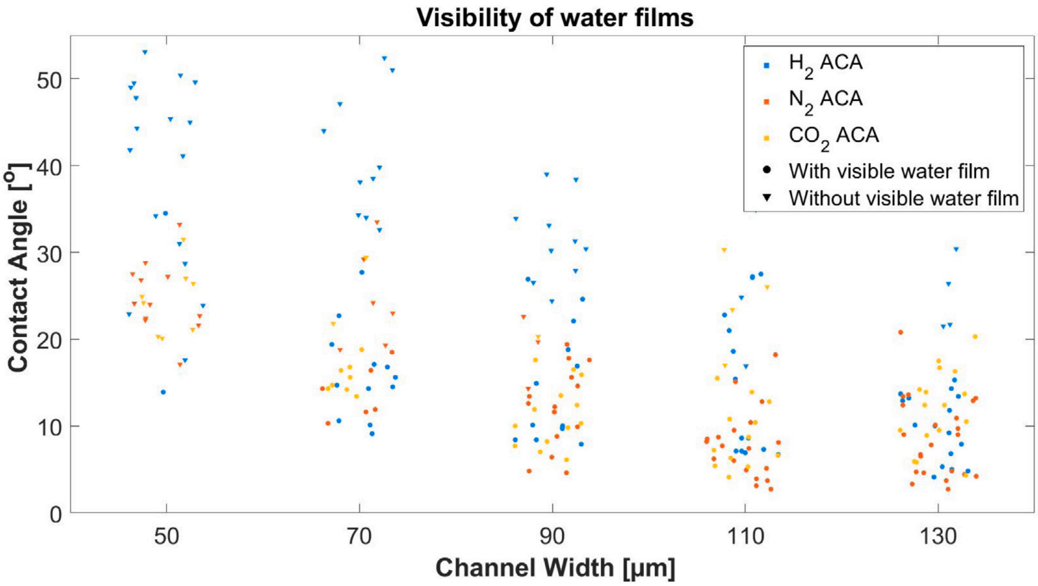

Fig. 9. Indication of the existence or nonexistence of a visible water film in advancing contact angle (ACA) measurements for H_2, N_2 and CO_2. Note that the smallest channel, i.e., 50 μm, has only a few cases with visible water films, while the visible water films almost always exist in the channel width of 130 μm.

provide a trend between contact angles and channel width. The trend resulting from the first approach, i.e., equal capillary pressure in rectangular pores, derived by Joekar Niasar et al. (2009) and explained in Eq. (D.1) Appendix D, does not fully match with our experimental observations. However, the trends found based on the second approach, i.e., constant velocities, as explained in Eq. (D.8) Appendix D, matched our experimental observations pretty well. This shows that, for our specific setup and experimental condition (unsteady state), it is highly unlikely that the capillary pressure is constant across channel widths. The scientific basis for the observed trend of our study, therefore, can be found by the fact that in average the velocities across the channel widths, in our experimental condition, are comparable.

4.3. Comparison between advancing and receding contact angles

Besides the spread of measurements mentioned in the previous section, there was no significant difference found between the advancing and receding contact angles. Contact angle hysteresis (the difference between advancing and receding contact angles) is the result of pore structure heterogeneity, chemical interactions between the fluid and solid rock surface, as well as surface roughness (Behnoudfar et al., 2022; Sauer and Carney, 1990; Tadmor, 2004; Morrow, 1975). The microchips used were made of smooth, pure borosilicate glass, and although the chip consisted of different channel widths there were no tapered structures that could lead to snap-off. Furthermore, the fluids used in the experiments were very pure since they were filtered before injection into the chip. No significant hysteresis is therefore expected. Surprisingly, the results of the work of Jafari and Jung (2017) did show contact angle hysteresis for the CO2/water system using the same chip. We believe, however, that this is likely the result of impurities in the system. This is discussed in detail in Appendix C, which shows that impurities can cause an increase in hysteresis of contact angles due to chemical/structural imperfections.

The systematic dependency of the advancing and receding contact angles on the intrinsic contact angle that Morrow (1975) found on roughened tubes was not observed in our measurements, because of the smooth channel walls of the microchip used in this experiment.

4.4. Comparison of gases

H_2/water, N_2/water, and CO_2/water systems behaved similarly during drainage when the receding contact angles were measured. However, a larger spread of measurements was observed in H_2 advancing contact angles in comparison to N_2 and CO_2 advancing contact angles. The minimum values of contact angles measured are similar for the three gases, while the maximum of the range of measurements of H_2 advancing contact angles is higher than N_2 and CO_2. This can be explained by the fact that more contact angles without water films

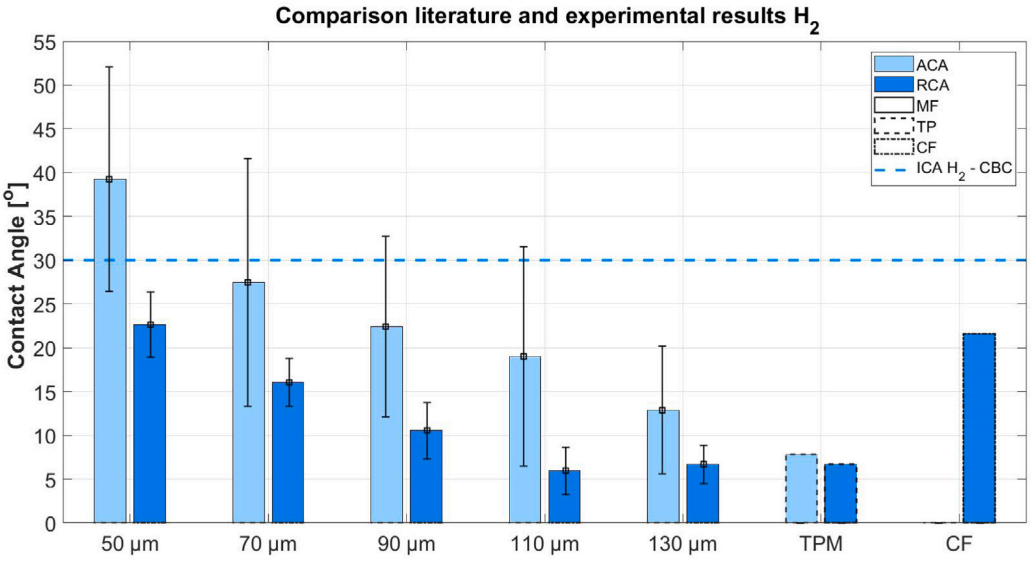

Fig. 10. H_2/water advancing and receding contact angles (ACA and RCA) for channel widths of 50 to 130 µm found by the microfluidic experiments of this study (MF). The results of the tilted plate method of Iglauer et al. (2021) (TPM), and the core flooding method of Yekta et al. (2018) (CF), are represented by the bars on the right. The dashed blue line represents the results found by Hashemi et al. (2021b) at P = 20 bar and T = 20 °C using the captive bubble cell (CBC). The error bars represent the standard deviation of the measurements.

were observed in the case of H_2, resulting in higher contact angles. The reason for this is currently unknown and will be part of our future work.

The similar wettability behaviour of CO_2 and N_2 has previously been observed using core-flooding experiments (Garing and Benson, 2019; Al-Menhali et al., 2015). The data on hydrogen wettability compared to other gases, however, is still limited. Note that the interfacial tension of H_2/water, N_2/water and CO_2/water at 10 bar and 25 °C are, respectively, 72.9, 71.4 and 65.7 mN/m (Yan et al., 2001; Chow et al., 2018; Georgiadis et al., 2010). These values are within 10% of each other. The close interfacial tension values could provide insight on the comparable contact angles found in our experiments. Note also to the point that in a gas/liquid interface, the neighbouring molecules of the liquid are all in close proximity, while the neighbouring molecules of the gas are relatively far away. Therefore, the energy of a molecule at the interface is expected to be mainly determined by the fluid phase, while the gas phase is expected to have little impact.

4.5. H_2 /water contact angles compared with literature

The bar plot of Fig. 10 compares the findings on H_2/water dynamic contact angles, both advancing and receding, with the currently available literature data on dynamic contact angles measured for this system. The dynamic contact angles for the H_2/water system measured with the microfluidic device of this study (Test A) for channel widths ranging from 50 to 130 µm are presented together with the H_2/brine/quartz results of the tilted plate experiment of Iglauer et al. (2021) (P = 50 bar, T = 23 °C and salinity = 100 000 ppm), referred to as TPM, and the H_2/water/sandstone core-flooding experiment of Yekta et al. (2018) (P = 50 bar and T = 20 °C), referred to as CF. In addition, the horizontal blue dashed line represents the intrinsic contact angle for the H_2/water/sandstone found by the captive-bubble experiments of Hashemi et al. (2021b) (P = 20 bar and T = 20 °C), referred to as CBC.

When comparing the results of Iglauer et al. (2021) with the results of our microfluidic experiment, it can be seen that the results of Iglauer et al. (2021) are similar to the results of the 130 µm channel. The receding contact angles are the same. The advancing contact angles, however, differ by 5°. In both experimental methods, the advancing contact angles are found to be less reproducible, which could explain the difference. The receding contact angle found by Yekta et al. (2018) is very similar to the receding contact angle measured in channels of 50 µm in width, with only 1° difference. Yekta et al. (2018) used a Vosges Sandstone for the core flooding experiment. It is possible that the common pore sizes in this sandstone are in the range of 50 µm.

5. Conclusions

Prediction of rock wettability in contact with brine and hydrogen is crucial for modelling the displacement processes in underground hydrogen storage (UHS). This paper reports experimental measurements of the advancing and receding contact angles of H_2/water, N_2/water and CO_2/water systems at P = 10 bar and T = 20 °C using a microfluidic device. The channel widths of the microfluidic chip, ranged between 50 and 130 µm, and the size of the smallest channel corresponds to the range of most common pore sizes found in typical sandstones (Hashemi et al., 2021a; Anon, 2022). Results of this study allow for more accurate design of pore-scale pore-network systems, as they require dynamic contact angles as input data. Furthermore, it can be used to understand the wide variation in the limited H_2/brine contact angle data which is currently reported. The results indicate water-wet conditions with H_2/water advancing contact angles ranging between 13–39°, and receding contact angles between 6 - 23°. The contact angles decreased with increasing channel widths. The receding contact angle measured for the smallest channel width (50 µm) is in agreement with the receding contact angle determined by Yekta et al. (2018) on the Vosges Sandstone, suggesting that this channel width could be representative of actual subsurface systems. The N_2/water and CO_2/water systems showed similar behaviour to the H_2/water system and no significant differences were observed for the three different gases.

CRediT authorship contribution statement

Willemijn van Rooijen: Methodology, Experiments, Writing – original draft. **Leila Hashemi:** Methodology, Experiments, Writing – review & editing. **Maartje Boon:** Methodology, Experiments, Writing – review & editing. **Rouhi Farajzadeh:** Methodology, Writing – review & editing. **Hadi Hajibeygi:** Conceptualization, Methodology, Writing – review & editing, Grant acquiring.

Declaration of competing interest

The authors declare that they have no known competing financial interests or personal relationships that could have appeared to influence the work reported in this paper.

Acknowledgements

Hadi Hajibeygi, Willemijn van Rooijen and Maartje Boon were sponsored by the Dutch National Science Foundation (NWO) Talent Programme ViDi Project "ADMIRE" (grant number 17509). We thank all ADMIRE members and its user committee for allowing us publish this paper. Groups members of DARSim (Delft Advanced Reservoir Simulation) and ADMIRE (Adaptive Dynamic Multiscale Integrated Reservoir Earth) are acknowledged for useful discussions during the development of this work. This study was conducted in the Laboratory of Geoscience and Engineering at Delft University of Technology. We gratefully thank the technical staff of the Laboratory, specially Michiel Slob. We also thank Dr. Sian Jones for her help in the laboratory during designing the setup. Lastly, authors would like to thank Professor Volkert van Steijn of TU Delft for fruitful discussions on gas/liquid/solid contact angle and interfacial tension.

Appendix A. Validation of setup

The setup was successfully calibrated against the existing literature data of Jafari and Jung (2017). They performed microfluidic measurements of advancing and receding contact angles of CO_2/Water at P = 10 bar and T = 21 °C using a chip identical to the chip used in this research. The cleaning method of Jafari and Jung was similar to our cleaning method. In order to match the setup of Jafari and Jung (2017), for the first validation test (V1) a setup without filters and valves was used. However, because knowledge was gained about the behaviour and sensitivities of the system (Appendix C), two additional CO_2/water tests (V2 and V3) were performed with the regular setup (presented in 2.3 Fig. 3). One test was done after saturating the water with CO_2, by filling the pump cylinders with half CO_2 and half pure water and leaving it overnight at a pressure of 20 bar. The other test was done with pure water. An overview of all validation tests and the test of Jafari and Jung can be found in Table A.3.

The results of the validation tests are shown in Fig. A.11. The orange bars represent the measurements of Jafari and Jung (2017) using a similar chip at P = 10 bar and T = 21 °C, the green, yellow and purple bars represent respectively validation experiments V1, V2 and V3, all carried out at P = 10 (±1) bar and$T$ = 20 (±2) °C.

Fig. A.11 shows that the results of experiment V1, using a similar setup, match the results of Jafari and Jung. The deviation is within the experimental error.

Fig. A.11 also indicates a clear effect of the filters in the setup on the advancing contact angles. When the system is not properly filtered, presence of contaminants can alter the glass wettability, resulting in an increase of advancing contact angles of up to 45°. This effect occurs especially when no valves are used, because the system has to be opened and closed for flushing before every experiment, which allows dust to attach on the open wet ends of the tubes. The effect on the receding contact angles is less evident. receding contact angles in unfiltered systems can be up to 5° higher, but this is still within the experimental error.

Lastly, when comparing the results of experiments V2 and V3, it can be seen that saturating the water with CO_2 had no significant influence on the results. This is in line with the finding that even though the water in experiment V1 was not saturated with CO_2, the results are still in agreement with the experiment of Jafari and Jung. The finding that saturating the water with a soluble gas like CO_2 does not impact the contact angle, confirms that pre-equilibrating the water during experiments with much less soluble gases, like H_2 and N_2, is not necessary, which is in agreement with Hashemi et al. (2022).

Appendix B. Validation of image analysis

The image analysis code was validated against the generated specific curvature using MATLAB with the known angles at the contact points. The accuracy of the developed in-house code is ±4° which is shown in Fig. B.12.

Appendix C. Sensitivity analysis: Contamination

It was found that surface contamination can alter the wettability of the system. This was initially found when unfiltered ethanol was injected and the system became clearly less water-wet. In order to investigate the effect that presence of contaminants can have on the dynamic contact angles, three experiments were performed. For the first test, Chip 1, 2 and 3 were used, which were all injected with the unfiltered ethanol instead of the filtered ethanol during the cleaning procedure. This resulted in severe contamination of the system. Furthermore, the chips were heated up to 400 °C in an (unsuccessful) attempt to clean the chip. The second test was done using chip 4. This chip was cleaned with the filtered ethanol, but some tests were done without the inline filters in the gas and water lines (Filters 2 and 3 in Fig. 3), which caused minor contamination. The third test was done with the unused chip, which was also cleaned with the filtered ethanol. Images of these chips can be seen in Fig. C.13. All chips were used for tests to investigate the influence of this contamination. Contact angles were only measured if there were no visible contamination particles in the vicinity of the interface.

Fig. C.14 shows the results of using different chips. The red bars represent the results of Chip 1–3, the green bars represent the results of chip 4 and the blue bars represent the results of chip 5. All experiments were carried out at P = 10 (±1) bar and T=20 (±2) °C.

Fig. C.14 indicates a clear effect of contamination on contact angles. It is clear that in Chip 1, 2 and 3, significantly higher advancing and receding contact angles were measured compared to chip 4 and 5. The difference between the results of chip 4 and chip 5 is less evident. The receding contact angles are very similar and the deviation are within the range of experimental error. The difference in advancing contact angles is more significant, but in most cases this is within experimental error as well. It is remarkable that the cleanest chip, chip 5, shows a wider range of advancing contact angles than chip 4. This is mainly because during imbibition experiments (measurement of advancing contact angle) in Chip 4, almost no water films were observed, while in Chip 5 the system was more water-wet because the chip was clean. In this case some interfaces used for advancing contact angle measurement had water films while others did not have a visible water film, like is shown in the images in Fig. 8.

Because a clear effect of contamination was found, even though contact angles were not measured within the vicinity of visible pollution,

Table A.3
Summary of the validation test Groups. Test Group JJ represents the results of Jafari and Jung (2017).

Test Group	Gas	Liquid	Rate [μl/min]	Temperature [°C]	Pressure [bar]	Comments
JJ	CO_2	Saturated Water	0.1	21	10	Setup without filters
V1	CO_2	Pure Water	0.1	20	10	Setup without filters and valves
V2	CO_2	Saturated Water	0.1	20	10	
V3	CO_2	Pure Water	0.1	20	10	

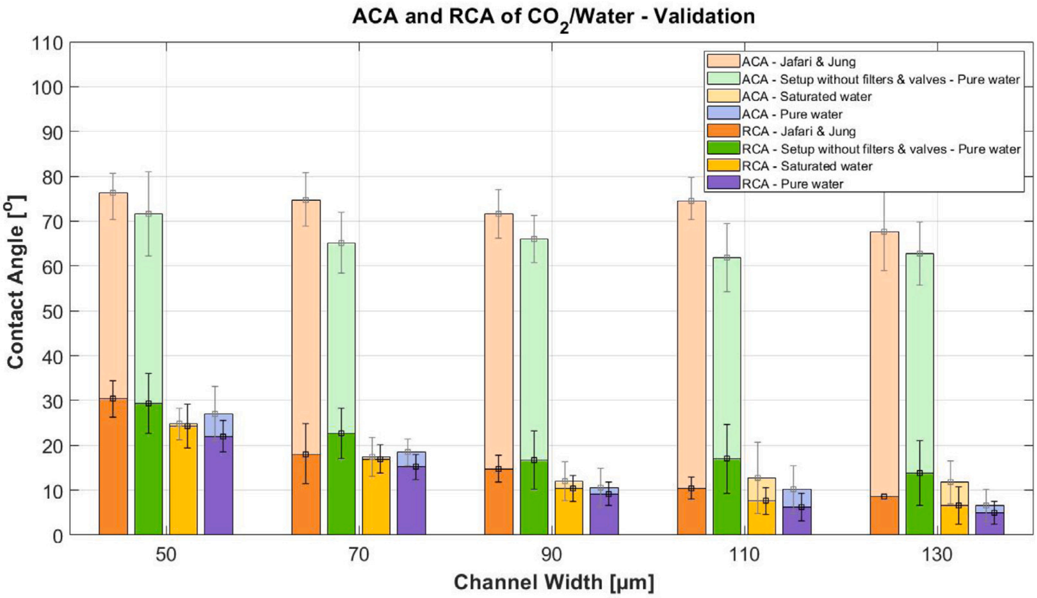

Fig. A.11. Advancing and receding contact angles (ACA and RCA) of CO_2/water systems. The orange bars represent the results of Jafari and Jung (2017) using a similar chip at P = 10 bar and T = 21 °C. The green bars represent results of V1 with a setup similar to Jafari and Jung without filters and valves and with pure water, the yellow bars represent the results of V2 with water which was saturated with CO_2 and the purple bars represent the results of V3 with pure water. The error bars represent the standard deviation of the measurements.

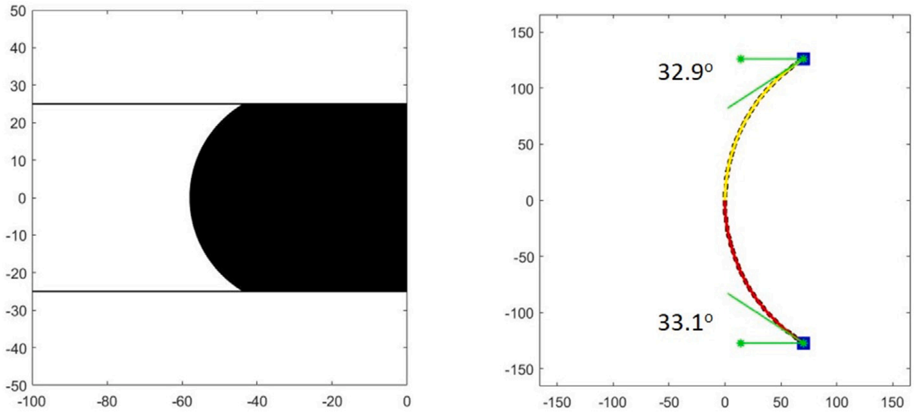

(a) Generated curvature of 30 ° (b) Fitted 6th order polynomial on curvature

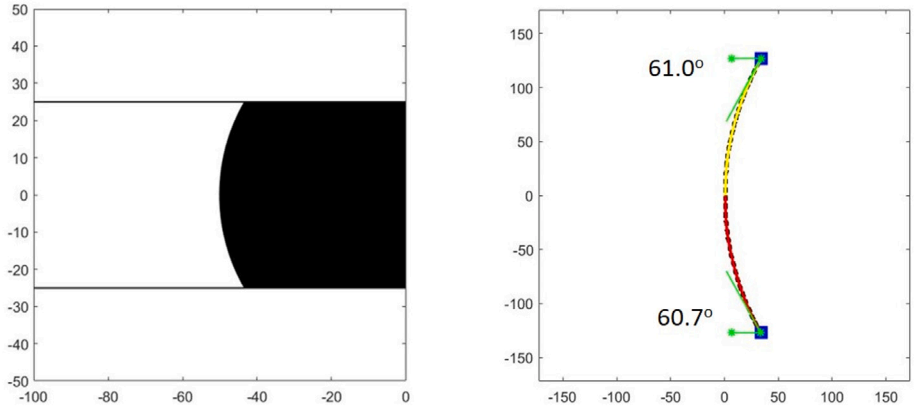

(c) Generated curvature of 60 ° (d) Fitted 6th order polynomial on curvature

Fig. B.12. Validation of the image analysis.

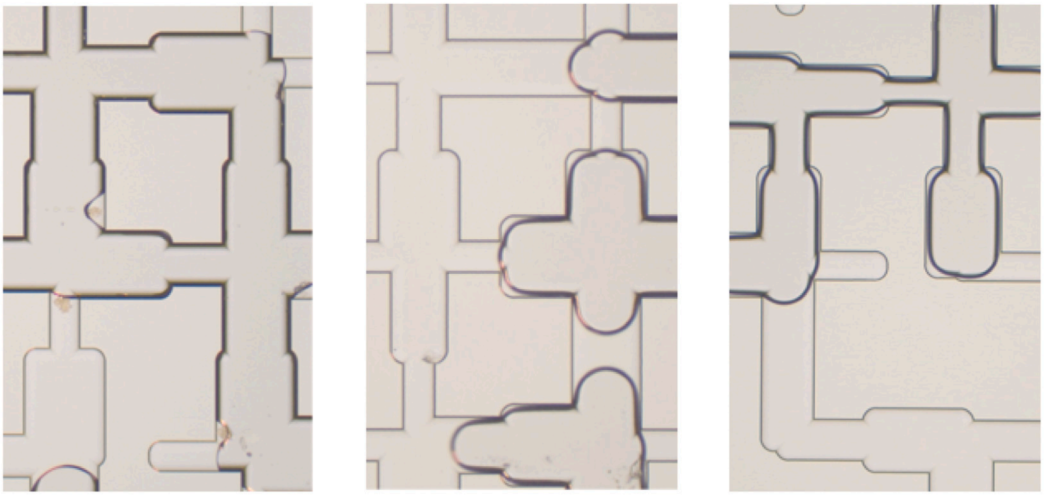

(a) Example of dirt in chip 1, 2 and 3. The chips are severely contaminated and the system is visibly less water-wet and there are no water films present

(b) Example of dirt in chip 4. A few dirt particles are visible, but the system is still very water wet and water films are observed

(c) Completely new chip, no dirt visible.

Fig. C.13. Examples of contamination and its effect on the wettability.

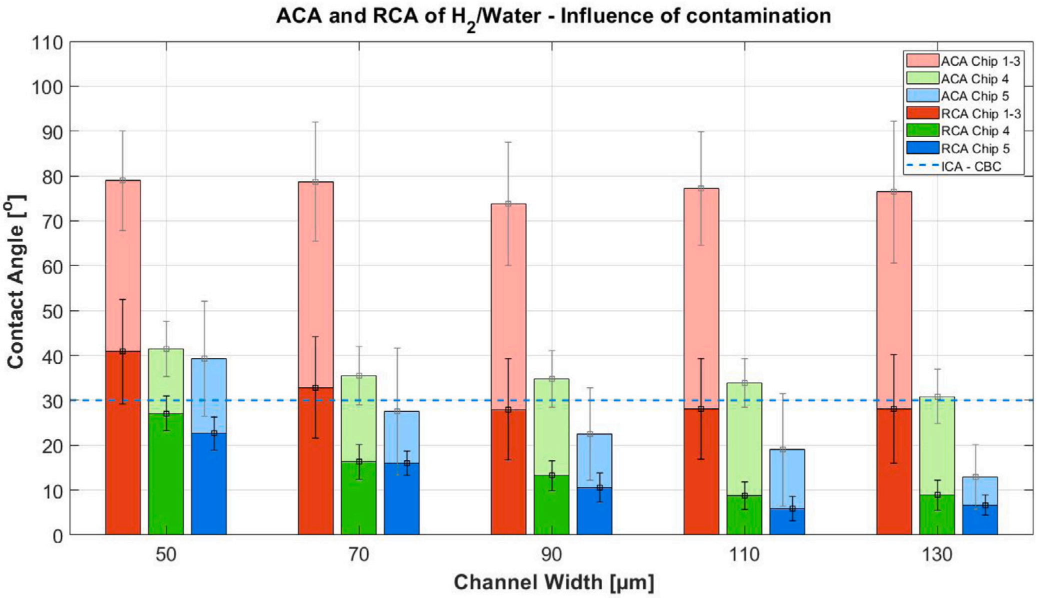

Fig. C.14. Advancing and receding contact angles (ACA and RCA) of H_2 and Pure water measured at P = 10 bar and T = 20 °C. The red bars represent measurements using chip 1, 2 and 3 which were severely contaminated, The green bars represent measurements using chip 4, which had minor contamination and the blue bars represent measurements using chip 5 which was clean. The dashed blue line represents the results found by Hashemi et al. (2021b) at P = 20 bar and T = 20 °C, using the captive bubble cell (CBC). The error bars are the standard deviation of all measurements.

all main experiments were carried out with filters, and only filtered fluids were injected. Furthermore, the system was opened inside the filters minimally in order to prevent dust from coming into the system. Installing valves 2 and 5 (Fig. 3) enabled this, since the lines did not have to be disconnected for flushing when using valves. The findings of this appendix are in line with the findings of the CO_2 experiments in Appendix A.

Appendix D. Sensitivity analysis: Velocity and channel width

For one of the H_2/water drainage experiments, the velocity of each specific interface was measured using ImageJ. Fig. D.15 shows the velocity distribution corresponding to the measured receding contact angles for different channel widths. No systematic relationship can be observed between receding contact angles and the velocity. This could possibly be explained by the fact that these measurements are influenced by many factors like local flow velocity, flow patterns, image analysis, image quality etc., which results in a relatively wide range of values.

Fig. D.16 shows the average velocity of the receding contact angles of this test, and the error bars represent the standard deviation of the measurements. It can be observed that similar velocities were measured for each channel width, which suggests that the dependency of contact angles on channel width was not due to differences in velocity. Instead, one can fairly conclude that the average velocities across channel widths are in fact comparable.

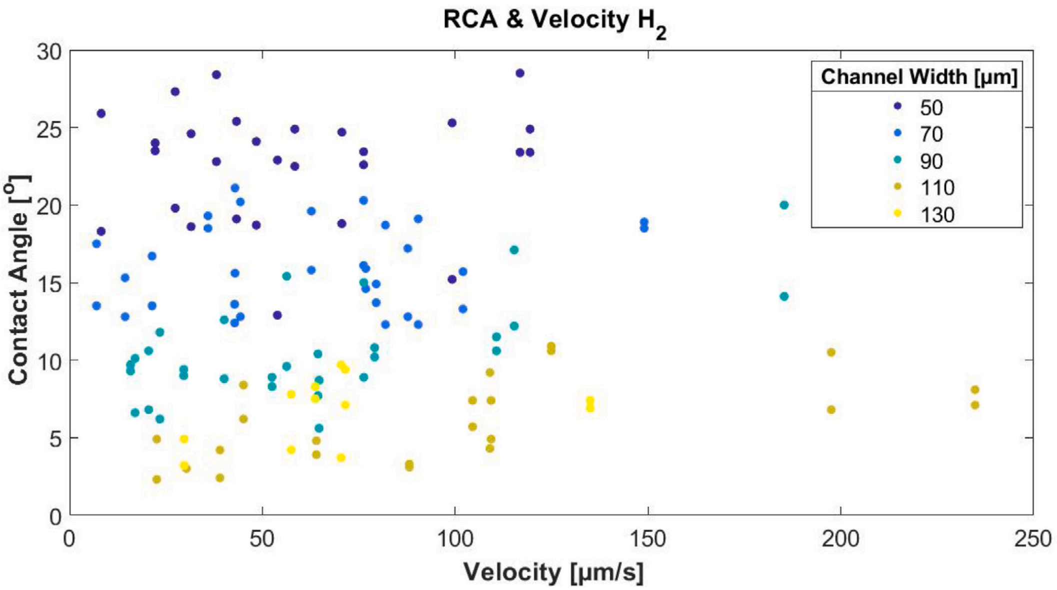

Fig. D.15. Velocity of receding contact angles (RCA) of H_2/water systems. Different colours represent measurements in different channel widths.

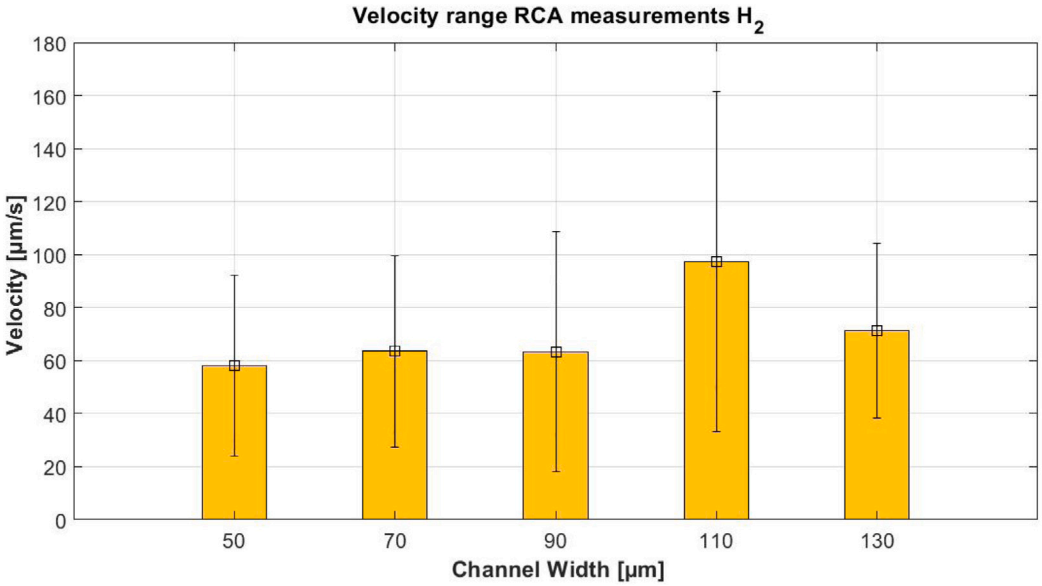

Fig. D.16. Velocity range of receding contact angles (RCA) of H_2/water systems per channel width. The bars represent the average velocity of the receding contact angles (RCA) measurements of this test, and the error bars represent the standard deviation of the velocity measurements.

The contact angles are expected to be influenced by the pore size (Behnoudfar et al., 2022; Rabbani et al., 2016, 2017). Our results show a relationship where dynamic contact angles increase with decreasing channel width, in agreement with the trend observed in the literature for CO_2 (Jafari and Jung, 2017). Multiple factors, like the shape of the channels, the capillary pressure and the velocity can influence the relationship between pore size and contact angles. Joekar Niasar et al. (2009) found that the capillary pressure in rectangular channels can be expressed as

$$P_c = \sigma_{nw} \left(\frac{-(h+w)\cos\theta + \sqrt{(h+w)^2\cos^2\theta + 4hw\left(\frac{\pi}{4} - \theta - \sqrt{2}\cos\left(\frac{\pi}{4}+\theta\right)\cos\theta\right)}}{4\left(\frac{\pi}{4} - \theta - \sqrt{2}\cos\left(\frac{\pi}{4}+\theta\right)\cos\theta\right)} \right)^{-1}, \tag{D.1}$$

where P_c is the capillary pressure, h is the channel depth and w is the channel width. The capillary pressure was calculated for a reference channel width, in this case 110 μm, using the measured contact angle θ. If the capillary pressure is assumed to be constant in the whole chip, because the regime is capillary dominated, the relationship between contact angles and channel width can be obtained by using the capillary pressure of the reference channel width and calculating the contact angles for other channel widths based on that value. However, because we deal with a dynamic system, where the capillary entry pressure needs be overcome in order for fluids to enter a channel, the assumption that capillary pressure is equal in each channel width, may not be valid. From Fig. D.16, one can conclude that the average velocities are comparable across channel widths. Berthier et al. (2015) proposed

$$P_c = \mu \frac{p_W z}{\bar{\lambda} S_{\mathrm{c}}} V \tag{D.2}$$

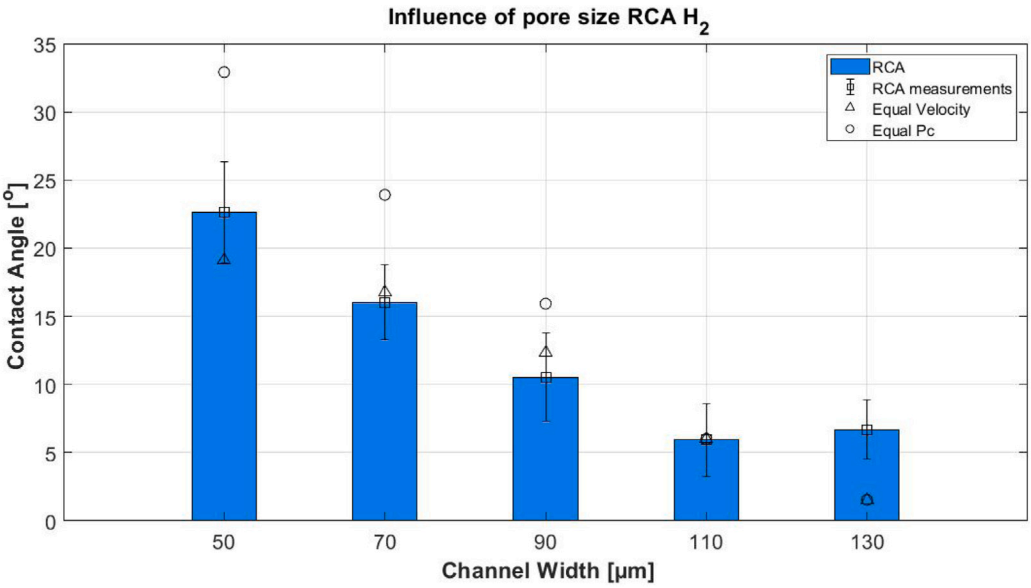

Fig. D.17. Receding contact angles (RCA) of H_2 and pure water measured at P = 10 bar and T = 20°. The triangles represent the expected relationship between contact angle and channel width assuming the velocity to be equal in each channel width, and the circles represent the expected relationship between contact angle and channel width assuming the capillary pressure to be equal in each channel width.

as the capillary pressure in rectangular channels, where

$$S_c = hw \tag{D.3}$$

$$p_W = 2(w + h) \tag{D.4}$$

$$\bar{\lambda} = \frac{\varepsilon q(\varepsilon)(w + h)}{2} \tag{D.5}$$

$$\varepsilon = h/w \tag{D.6}$$

$$q(\varepsilon) = \frac{1}{3} - \frac{64}{\pi^5}\varepsilon \tanh\left(\frac{\pi}{2\varepsilon}\right). \tag{D.7}$$

Here, μ is the viscosity and z is the distance from the inlet of the channel to the interface. Using the fact that in our experiments velocities across the channel widths are comparable ($V_i = V_{ref}$), and assuming that z is on average similar for each channel width, the equation can be rewritten as

$$\frac{P_{c_{ref}}\bar{\lambda}_{ref}S_{c_{ref}}}{p_{W_{ref}}} = \frac{P_{c_i}\bar{\lambda}_{r_i}S_{c_i}}{p_{W_i}}. \tag{D.8}$$

The left-hand-side term of this equations represents the velocity factor for the reference channel width. The capillary pressure $P_{c_{ref}}$ is calculated using Eq. (D.1). Eq. (D.8) was used to derive contact angle values for the other channel widths, using Eq. (D.1) to calculate P_{c_i}. The calculated contact angles represent the relationship between contact angle and channel width based on the assumption that velocity is equal in each channel width.

Fig. D.17 shows the average receding contact angles (RCA) of H_2 and pure water measurements. The triangles represent the expected relationship between contact angle and channel width assuming the velocity is equal for each channel width, and the circles represent the values assuming the capillary pressure is equal for all channel widths. For both relationships, the contact angle of the channel width of 110 μm was used as a reference point. It can be observed that the relationship assuming equal velocity resembles the measurements more closely.

References

Al-Menhali, A., Niu, B., Krevor, S., 2015. Capillarity and wetting of carbon dioxide and brine during drainage in b erea sandstone at reservoir conditions. Water Resour. Res. 51 (10), 7895–7914. http://dx.doi.org/10.1002/2015WR016947.

Al-Zaidi, E., Fan, X., 2018. Effect of aqueous electrolyte concentration and valency on contact angle on flat glass surfaces and inside capillary glass tubes. Colloids Surf. A 543, 1–8. http://dx.doi.org/10.1016/j.colsurfa.2018.01.045.

Alhammadi, A.M., AlRatrout, A., Singh, K., Bijeljic, B., Blunt, M.J., 2017. In situ characterization of mixed-wettability in a reservoir rock at subsurface conditions. Sci. Rep. 7 (1), 1–9. http://dx.doi.org/10.1038/s41598-017-10992-w.

Ali, M., Jha, N.K., Al-Yaseri, A., Zhang, Y., Iglauer, S., Sarmadivaleh, M., 2021. Hydrogen wettability of quartz substrates exposed to organic acids; implications for hydrogen trapping/storage in sandstone reservoirs. J. Pet. Sci. Eng. 109081. http://dx.doi.org/10.1029/2020GL090814.

Anon, 2022. Micro-CT images and networks. http://www.imperial.ac.uk/earth-science/research/research-groups/perm/research/pore-scale-modelling/micro-ct-images-and-networks.

Arif, M., Lebedev, M., Barifcani, A., Iglauer, S., 2017. Co2 storage in carbonates: Wettability of calcite. Int. J. Greenh. Gas Control 62, 113–121. http://dx.doi.org/10.1016/j.petrol.2021.108679.

Bear, J., 2013. Dynamics of Fluids in Porous Media. Courier Corporation.

Behnoudfar, D., Dragila, M.I., Meisenheimer, D., Wildenschild, D., 2022. Contact angle hysteresis: A new paradigm? Adv. Water Resour. 104138. http://dx.doi.org/10.1016/j.advwatres.2022.104138.

Berthier, J., Gosselin, D., Berthier, E., 2015. A generalization of the Lucas–Washburn–Rideal law to composite microchannels of arbitrary cross section. Microfluid. Nanofluid. 19 (3), 497–507. http://dx.doi.org/10.1007/s10404-014-1519-3.

Blunt, M.J., 2017. Multiphase Flow in Permeable Media: A Pore-Scale Perspective. Cambridge University Press.

Blunt, M.J., Jackson, M.D., Piri, M., Valvatne, P.H., 2002. Detailed physics, predictive capabilities and macroscopic consequences for pore-network models of multiphase flow. Adv. Water Resour. 25 (8–12), 1069–1089. http://dx.doi.org/10.1016/S0309-1708(02)00049-0.

Carden, P., Paterson, L., 1979. Physical, chemical and energy aspects of underground hydrogen storage. Int. J. Hydrogen Energy 4 (6), 559–569. http://dx.doi.org/10.1016/0360-3199(79)90083-1.

Castro, E.R., Tarn, M.D., Ginterová, P., Zhu, H., Xu, Y., Neužil, P., 2018. Determination of dynamic contact angles within microfluidic devices. Microfluid. Nanofluid. 22 (5), 1–11. http://dx.doi.org/10.1007/s10404-018-2066-0.

Celia, M.A., Reeves, P.C., Ferrand, L.A., 1995. Recent advances in pore scale models for multiphase flow in porous media. Rev. Geophys. 33 (S2), 1049–1057. http://dx.doi.org/10.1029/95RG00248.

Chalbaud, C., Robin, M., Lombard, J., Martin, F., Egermann, P., Bertin, H., 2009. Interfacial tension measurements and wettability evaluation for geological CO2 storage. Adv. Water Resour. 32 (1), 98–109. http://dx.doi.org/10.1016/j.advwatres.2008.10.012.

Cheng, J.-T., Pyrak-Nolte, L.J., Nolte, D.D., Giordano, N.J., 2004. Linking pressure and saturation through interfacial areas in porous media. Geophys. Res. Lett. 31 (8), http://dx.doi.org/10.1029/2003GL019282.

Chow, Y.F., Maitland, G.C., Trusler, J.M., 2018. Interfacial tensions of (H2O+ H2) and (H2O+ CO2+ H2) systems at temperatures of (298–448) K and pressures up to 45 MPa. Fluid Phase Equilib. 475, 37–44. http://dx.doi.org/10.1016/j.fluid.2018.07.022.

Constantinides, G.N., Payatakes, A.C., 1996. Network simulation of steady-state two-phase flow in consolidated porous media. AIChE J. 42 (2), 369–382. http://dx.doi.org/10.1002/aic.690420207.

Dalton, L.E., Tapriyal, D., Crandall, D., Goodman, A., Shi, F., Haeri, F., 2020. Contact angle measurements using sessile drop and micro-ct data from six sandstones. Transp. Porous Media 133 (1), http://dx.doi.org/10.1007/s11242-020-01415-y.

Darzi, M., Park, C., 2017. Optical distortion correction of a liquid-gas interface and contact angle in cylindrical tubes. Phys. Fluids 29 (5), 052004. http://dx.doi.org/10.1063/1.4982902.

Dickson, J.L., Gupta, G., Horozov, T.S., Binks, B.P., Johnston, K.P., 2006. Wetting phenomena at the CO2/water/glass interface. Langmuir 22 (5), 2161–2170. http://dx.doi.org/10.1021/la0527238.

Dong, H., Fjeldstad, S., Alberts, L., Roth, S., Bakke, S., Øren, P.-E., et al., 2008. Pore network modelling on carbonate: a comparative study of different micro-CT network extraction methods. In: International Symposium of the Society of Core Analysts, Society of Core Analysts.

Espinoza, D.N., Santamarina, J.C., 2010. Water-CO2-mineral systems: Interfacial tension, contact angle, and diffusion—Implications to CO2 geological storage. Water Resour. Res. 46 (7), http://dx.doi.org/10.1029/2009WR008634.

Ferer, M., Ji, C., Bromhal, G.S., Cook, J., Ahmadi, G., Smith, D.H., 2004. Crossover from capillary fingering to viscous fingering for immiscible unstable flow: Experiment and modeling. Phys. Rev. E 70 (1), 016303.

Garing, C., Benson, S., 2019. Co2 wettability of sandstones: Addressing conflicting capillary behaviors. Geophys. Res. Lett. 46 (2), 776–782. http://dx.doi.org/10.1029/2018GL081359.

Georgiadis, A., Maitland, G., Trusler, J.M., Bismarck, A., 2010. Interfacial tension measurements of the (H2O+ CO2) system at elevated pressures and temperatures. J. Chem. Eng. Data 55 (10), 4168–4175. http://dx.doi.org/10.1021/je100198g.

Godinez-Brizuela, O.E., Karadimitriou, N.K., Joekar-Niasar, V., Shore, C.A., Oostrom, M., 2017. Role of corner interfacial area in uniqueness of capillary pressure-saturation-interfacial area relation under transient conditions. Adv. Water Resour. 107, 10–21. http://dx.doi.org/10.1016/j.advwatres.2017.06.007.

Gunda, N.S.K., Bera, B., Karadimitriou, N.K., Mitra, S.K., Hassanizadeh, S.M., 2011. Reservoir-on-a-chip (ROC): A new paradigm in reservoir engineering. Lab on A Chip 11 (22), 3785–3792. http://dx.doi.org/10.1039/C1LC20556K.

Gutiérrez, B., Juarez, F., Ornelas, L., Zeppieri, S., De Ramos, A.L., 2008. Experimental study of gas–liquid two-phase flow in glass micromodels. Int. J. Thermophys. 29 (6), 2126–2135. http://dx.doi.org/10.1007/s10765-007-0305-9.

Hashemi, L., Blunt, M., Hajibeygi, H., 2021a. Pore-scale modelling and sensitivity analyses of hydrogen-brine multiphase flow in geological porous media. Sci. Rep. 11 (1), 1–13. http://dx.doi.org/10.1038/s41598-021-87490-7.

Hashemi, L., Boon, M., Glerum, W., Farajzadeh, R., Hajibeygi, H., 2022. A comparative study for H2-CH4 mixture wettability in sandstone porous rocks relevant to underground hydrogen storage. Adv. Water Resour. 104165. http://dx.doi.org/10.1016/j.advwatres.2022.104165.

Hashemi, L., Glerum, W., Farajzadeh, R., Hajibeygi, H., 2021b. Contact angle measurement for hydrogen/brine/sandstone system using captive-bubble method relevant for underground hydrogen storage. Adv. Water Resour. 103964. http://dx.doi.org/10.1016/j.advwatres.2014.02.014.

Heinemann, N., Alcalde, J., Miocic, J.M., Hangx, S.J., Kallmeyer, J., Ostertag-Henning, C., Hassanpouryouzband, A., Thaysen, E.M., Strobel, G.J., Schmidt-Hattenberger, C., et al., 2021. Enabling large-scale hydrogen storage in porous media–the scientific challenges. Energy Environ. Sci. http://dx.doi.org/10.1039/D0EE03536J.

Heiskanen, V., Marjanen, K., Kallio, P., 2008. Machine vision based measurement of dynamic contact angles in microchannel flows. J. Bionic Eng. 5 (4), 282–290. http://dx.doi.org/10.1016/S1672-6529(08)60172-9.

Heshmati, M., Piri, M., 2014. Experimental investigation of dynamic contact angle and capillary rise in tubes with circular and noncircular cross sections. Langmuir 30 (47), 14151–14162. http://dx.doi.org/10.1021/la501724y.

Higgs, S., Da Wang, Y., Sun, C., Ennis-King, J., Jackson, S.J., Armstrong, R.T., Mostaghimi, P., 2022. In-situ hydrogen wettability characterisation for underground hydrogen storage. Int. J. Hydrogen Energy.

Hirasaki, G., 1991. Wettability: fundamentals and surface forces. SPE Form. Eval. 6 (02), 217–226. http://dx.doi.org/10.2118/17367-PA.

Hu, R., Wan, J., Kim, Y., Tokunaga, T.K., 2017. Wettability effects on supercritical CO2–brine immiscible displacement during drainage: Pore-scale observation and 3D simulation. Int. J. Greenh. Gas Control 60, 129–139. http://dx.doi.org/10.1016/j.ijggc.2017.03.011.

Iglauer, S., Ali, M., Keshavarz, A., 2021. Hydrogen wettability of sandstone reservoirs: Implications for hydrogen geo-storage. Geophys. Res. Lett. 48 (3), http://dx.doi.org/10.1029/2020GL090814, e2020GL090814.

Jafari, M., Jung, J., 2017. Direct measurement of static and dynamic contact angles using a random micromodel considering geological CO2 sequestration. Sustainability 9 (12), 2352. http://dx.doi.org/10.3390/su9122352.

Joekar-Niasar, V., Hassanizadeh, S., 2012. Analysis of fundamentals of two-phase flow in porous media using dynamic pore-network models: A review. Crit. Rev. Environ. Sci. Technol. 42 (18), 1895–1976. http://dx.doi.org/10.1080/10643389.2011.574101.

Joekar Niasar, V., Hassanizadeh, S., Pyrak-Nolte, L., Berentsen, C., 2009. Simulating drainage and imbibition experiments in a high-porosity micromodel using an unstructured pore network model. Water Resour. Res. 45 (2), http://dx.doi.org/10.1029/2007WR006641.

Juanes, R., Spiteri, E., Orr Jr., F., Blunt, M., 2006. Impact of relative permeability hysteresis on geological CO2 storage. Water Resour. Res. 42 (12), http://dx.doi.org/10.1029/2005WR004806.

Karadimitriou, N., Hassanizadeh, S., 2012. A review of micromodels and their use in two-phase flow studies. Vadose Zone J. 11 (3), http://dx.doi.org/10.2136/vzj2011.0072.

Karadimitriou, N.K., Joekar-Niasar, V., Babaei, M., Shore, C.A., 2016. Critical role of the immobile zone in non-fickian two-phase transport: A new paradigm. Environ. Sci. Technol. 50 (8), 4384–4392. http://dx.doi.org/10.1021/acs.est.5b05947.

Karadimitriou, N.K., Joekar-Niasar, V., Brizuela, O.G., 2017. Hydro-dynamic solute transport under two-phase flow conditions. Sci. Rep. 7 (1), 1–7. http://dx.doi.org/10.1038/s41598-017-06748-1.

Karadimitriou, N.K., Mahani, H., Steeb, H., Niasar, V., 2019. Nonmonotonic effects of salinity on wettability alteration and two-phase flow dynamics in PDMS micromodels. Water Resour. Res. 55 (11), 9826–9837. http://dx.doi.org/10.1029/2018WR024252.

Kim, J.-H., Kavehpour, H.P., Rothstein, J.P., 2015. Dynamic contact angle measurements on superhydrophobic surfaces. Phys. Fluids 27 (3), 032107. http://dx.doi.org/10.1063/1.4915112.

Kim, Y., Wan, J., Kneafsey, T.J., Tokunaga, T.K., 2012. Dewetting of silica surfaces upon reactions with supercritical CO2 and brine: pore-scale studies in micromodels. Environ. Sci. Technol. 46 (7), 4228–4235. http://dx.doi.org/10.1021/es204096w.

Kunz, P., Hassanizadeh, S., Nieken, U., 2018. A two-phase SPH model for dynamic contact angles including fluid–solid interactions at the contact line. Transp. Porous Media 122 (2), 253–277. http://dx.doi.org/10.1007/s11242-018-1002-9.

Li, X., Fan, X., Askounis, A., Wu, K., Sefiane, K., Koutsos, V., 2013. An experimental study on dynamic pore wettability. Chem. Eng. Sci. 104, 988–997. http://dx.doi.org/10.1016/j.ces.2013.10.026.

MacKay, D., 2008. Sustainable Energy-Without the Hot Air. UIT cambridge.

Morrow, N.R., 1975. The effects of surface roughness on contact: angle with special reference to petroleum recovery. J. Can. Pet. Technol. 14 (04), http://dx.doi.org/10.2118/75-04-04.

Øren, P.-E., Bakke, S., 2003. Reconstruction of berea sandstone and pore-scale modelling of wettability effects. J. Pet. Sci. Eng. 39 (3–4), 177–199. http://dx.doi.org/10.1016/S0920-4105(03)00062-7.

Oren, P.-E., Bakke, S., Arntzen, O.J., 1998. Extending predictive capabilities to network models. SPE J. 3 (04), 324–336. http://dx.doi.org/10.2118/52052-PA.

Pan, B., Yin, X., Ju, Y., Iglauer, S., 2021. Underground hydrogen storage: Influencing parameters and future outlook. Adv. Colloid Interface Sci. 102473. http://dx.doi.org/10.1016/j.cis.2021.102473.

Patzek, T.W., 2001. Verification of a complete pore network simulator of drainage and imbibition. Spe J. 6 (02), 144–156. http://dx.doi.org/10.2118/71310-PA.

Peksa, A.E., Wolf, K.-H.A., Zitha, P.L., 2015. Bentheimer sandstone revisited for experimental purposes. Mar. Pet. Geol. 67, 701–719. http://dx.doi.org/10.1016/j.marpetgeo.2015.06.001.

Porter, M.L., Jiménez-Martínez, J., Martinez, R., McCulloch, Q., Carey, J.W., Viswanathan, H.S., 2015. Geo-material microfluidics at reservoir conditions for subsurface energy resource applications. Lab on A Chip 15 (20), 4044–4053. http://dx.doi.org/10.1039/C5LC00704F.

Rabbani, H.S., Joekar-Niasar, V., Pak, T., Shokri, N., 2017. New insights on the complex dynamics of two-phase flow in porous media under intermediate-wet conditions. Sci. Rep. 7 (1), 1–7. http://dx.doi.org/10.1038/s41598-017-04545-4.

Rabbani, H.S., Joekar-Niasar, V., Shokri, N., 2016. Effects of intermediate wettability on entry capillary pressure in angular pores. J. Colloid Interface Sci. 473, 34–43. http://dx.doi.org/10.1016/j.jcis.2016.03.053.

Rapp, B.E., 2016. Microfluidics: Modeling, Mechanics and Mathematics. William Andrew, http://dx.doi.org/10.1016/C2012-0-02230-2.

Rücker, M., Bartels, W.-B., Singh, K., Brussee, N., Coorn, A., van der Linde, H.A., Bonnin, A., Ott, H., Hassanizadeh, S.M., Blunt, M.J., et al., 2019. The effect of mixed wettability on pore-scale flow regimes based on a flooding experiment in ketton limestone. Geophys. Res. Lett. 46 (6), 3225–3234. http://dx.doi.org/10.1029/2018GL081784.

Ryazanov, A.V., Van Dijke, M.I.J., Sorbie, K.S., 2009. Two-phase pore-network modelling: existence of oil layers during water invasion. Transp. Porous Media 80 (1), 79–99. http://dx.doi.org/10.1007/s11242-009-9345-x.

Saraji, S., Piri, M., Goual, L., 2014. The effects of SO2 contamination, brine salinity, pressure, and temperature on dynamic contact angles and interfacial tension of supercritical CO2/brine/quartz systems. Int. J. Greenh. Gas Control 28, 147–155. http://dx.doi.org/10.1017/9781316145098.

Sauer, B.B., Carney, T.E., 1990. Dynamic contact angle measurements on glass fibers: influence of fiber diameter on hysteresis and contact line pinning. Langmuir 6 (5), 1002–1007. http://dx.doi.org/10.1021/la00095a020.

Sharbatian, A., Abedini, A., Qi, Z., Sinton, D., 2018. Full characterization of CO2–oil properties on-chip: solubility, diffusivity, extraction pressure, miscibility, and contact angle. Anal. Chem. 90 (4), 2461–2467. http://dx.doi.org/10.1021/acs.analchem.7b05358.

Song, W., de Haas, T.W., Fadaei, H., Sinton, D., 2014. Chip-off-the-old-rock: the study of reservoir-relevant geological processes with real-rock micromodels. Lab on A Chip 14 (22), 4382–4390. http://dx.doi.org/10.1039/C1LC20556K.

Sun, C., McClure, J.E., Mostaghimi, P., Herring, A.L., Shabaninejad, M., Berg, S., Armstrong, R.T., 2020. Linking continuum-scale state of wetting to pore-scale contact angles in porous media. J. Colloid Interface Sci. 561, 173–180. http://dx.doi.org/10.1021/la501724y.

Tadmor, R., 2004. Line energy and the relation between advancing, receding, and young contact angles. Langmuir 20 (18), 7659–7664. http://dx.doi.org/10.1021/la049410h.

Yan, W., Zhao, G.-Y., Chen, G.-J., Guo, T.-M., 2001. Interfacial tension of (methane+ nitrogen)+ water and (carbon dioxide+ nitrogen)+ water systems. J. Chem. Eng. Data 46 (6), 1544–1548. http://dx.doi.org/10.1021/je0101505.

Yekta, A., Manceau, J.-C., Gaboreau, S., Pichavant, M., Audigane, P., 2018. Determination of hydrogen–water relative permeability and capillary pressure in sandstone: application to underground hydrogen injection in sedimentary formations. Transp. Porous Media 122 (2), 333–356. http://dx.doi.org/10.1007/s11242-018-1004-7.

Yusibani, E., Nagahama, Y., Kohno, M., Takata, Y., Woodfield, P.L., Shinzato, K., Fujii, M., 2011. A capillary tube viscometer designed for measurements of hydrogen gas viscosity at high pressure and high temperature. Int. J. Thermophys. 32 (6), 1111–1124.

Zhang, C., Oostrom, M., Wietsma, T.W., Grate, J.W., Warner, M.G., 2011. Influence of viscous and capillary forces on immiscible fluid displacement: Pore-scale experimental study in a water-wet micromodel demonstrating viscous and capillary fingering. Energy Fuels 25 (8), 3493–3505. http://dx.doi.org/10.1021/ef101732k.

Zivar, D., Kumar, S., Foroozesh, J., 2020. Underground hydrogen storage: A comprehensive review. Int. J. Hydrogen Energy http://dx.doi.org/10.1016/j.ijhydene.2020.08.138.